Mechanics Research Communications 154 (2026) 104671

Contents lists available at ScienceDirect

Mechanics Research Communications

journal homepage: www.elsevier.com/locate/mechrescom

Combining X-ray tomography and digital volume correlation to measure 3D bulk mechanical fields in Hertzian contact mechanics☆

Sylvain Dancette [b,*], Vito Acito [a,b], Jérome Adrien [b], Joël Lachambre [b], Eric Maire [b], Julien Scheibert [a], Davy Dalmas [a]

[a] CNRS, Ecole Centrale de Lyon, ENTPE, LTDS, UMR5513, 69134 Ecully, France
[b] Univ Lyon, INSA Lyon, CNRS UMR5510, Laboratoire MATEIS, Villeurbanne, F-69621, France

ARTICLE INFO

Keywords:
X-ray tomography
Digital volume correlation (DVC)
Hertzian contact mechanics

ABSTRACT

In this study, we revisit classical Hertzian contact theory through a novel experimental approach that enables in situ 3D imaging of contact mechanics using laboratory-based X-ray tomography. By employing a model contact system — a PDMS sphere indented into a PMMA plane — we measure the 3D displacement field within the deforming elastomeric PDMS sample during indentation using digital volume correlation (DVC). We introduce multiple methods to experimentally evaluate the stress field beneath the contact surface and directly compare it to the predicted Hertzian stress distribution. Our approach leverages DVC-based finite element simulations, where boundary conditions are fully derived from the experimentally measured displacement field. This eliminates reliance on contact assumptions or numerical contact algorithms, ensuring that the stress field is determined solely by experimental data. To our knowledge, this work presents the first experimentally driven characterization of a full-field stress distribution beneath the contact surface, demonstrating qualitative agreement with classical contact models. However, our findings also indicate that achieving quantitative agreement will require the development of more complex models, which do not currently exist, as well as advancements in DVC regularization schemes to account for surface-specific behaviors. While this paper focuses on normal loading conditions, the experimental setup and methodology are fully adaptable to any type of contact loading scenario.

1. Introduction

The mechanics of Hertzian contact is now more than 140 years old, with the original formulation of the theory of contact by Hertz [1], which considers the normal contact between two linearly elastic spheres, in the absence of friction or adhesion. A few decades later, Huber [2] was the first to establish the corresponding stress field inside the bulk of the contacting solids. Cattaneo [3] and Mindlin [4] derived the tangential stress field at the contact interface during the partial-slip-based incipient sliding, when an increasing shear load is imposed, under the assumption of a Coulomb-like friction law. Hamilton and Goodman [5] then Hamilton [6] later established the equations for the stress field in the bulk of the deformable body under fully sliding spherical contact and Coulomb friction.

These pioneering theories have been validated and extended later to various contexts, including for example the one of adhesive contact (Johnson et al. [7], Derjaguin et al. [8], Maugis [9]). However, despite the significant number of analytical or numerical contact models available today in the literature (see Müser et al. [10] for a comparison of models and Vakis et al. [11] for a review), the experimental measurement of the quantities at play during contact remains a challenging topic. This is due to the difficulty in accessing the confined contact region and the inside of the deforming bodies in contact. Most in-situ experimental techniques to date have been using optics-based methods, looking at contact from the top, exploiting the optical transparency of at least one of the two materials in contact. They focused on two main aspects of the contact: the contact area using e.g. binarization of the contact images (see examples in Dieterich and Kilgore [12], Sahli et al. [13], Acito et al. [14], Lengiewicz et al. [15], Zhang et al. [16]) and the interfacial in-plane displacement field using e.g. Digital Image Correlation (see examples in Prevost et al. [17], Tuononen [18]) or Particle Tracking Velocimetry (see examples in Chateauminois and Fretigny [19], Chateauminois et al. [20]).

☆ This article is part of a Special issue entitled: 'Lebensohn SI_invited only' published in Mechanics Research Communications.

* Corresponding author.
E-mail address: sylvain.dancette@insa-lyon.fr (S. Dancette).

https://doi.org/10.1016/j.mechrescom.2026.104671
Received 29 October 2025; Received in revised form 4 February 2026; Accepted 4 March 2026
Available online 5 March 2026

Recently, the advent of non-destructive 3D imaging techniques such as X-ray computed tomography (XRCT) [21,22] offered new perspectives to overcome the limits of optics-based techniques in the analysis of contact. Kriston et al. [23] used XRCT and image processing to analyze the rough contact area of rubber with various counter-surfaces under normal loading. Zhang et al. [24] and Zhang et al. [25] similarly used XRCT to analyze contact area and contact surface separation for non-transparent, rough metallic surfaces. In our previous study (Acito et al. [26]), we tried to quantify the limits of XRCT to measure the real contact area and extract the 3D surface displacement field in a model sphere-on-plate contact system. These 3D measurements were compared to the predictions of most used models of adhesive contact [27,28].

While the experimental efforts introduced above remained mostly focused on the measurement of quantities related to contact area or to the interfacial in-plane displacements, the recent extension of the digital image correlation (DIC) technique to 3D XRCT images [29] offers additional perspectives towards the non-destructive measurement of mechanical fields not just at the very interface, but inside the bulks of the deformable bodies. This was recently explored in Lachambre et al. [30], where digital volume correlation (DVC) was used to measure the displacement and strain fields in the bulk of a flat rubber sample with 10% silica particles, indented by a much stiffer polycarbonate sphere. These experimental fields (displacement and strain, noting the absence of stress measurement) were successfully compared to the predictions of an axisymmetric finite element model of contact.

Parallel to the development of XRCT and digital image/volume correlation, experimental techniques based on photoelasticity have been developed for materials exhibiting the proper birefringent properties, loaded under Hertzian contact conditions [31,32]. Setups based on photoelasticity constitute so far, to the best of the authors knowledge, the only published experimental studies allowing full-field assessment of bulk stresses in the context of Hertzian contact mechanics. They are however limited to birefringent materials and require moreover particular stress states such as plane stress or axisymmetry.

The objective of the present study is to establish an experimental workflow, as a proof of concept, allowing to perform three-dimensional, non-destructive measurements of sub-surface mechanical fields in the context of Hertzian contact mechanics. The goal is to enable direct, quantitative comparison of the fields measured experimentally with the ones available in the Hertzian theory of contact, taken here in the form of Hamilton's explicit equations for stresses beneath the contact surface [6]. To this end, we will first present the model sphere-on-plane contact system investigated, based on an elastomeric PDMS hemisphere in contact with a stiff PMMA plate. We will then introduce the *in situ* tribometer designed for this work, which allows to perform normal contact experiments within a laboratory X-ray tomograph. Details of the digital volume correlation procedure will then be given, before presenting the strategies adopted to assess the 3D strain and stress fields thanks to DVC. Systematic comparisons of the displacement, strain and stress fields between Hertzian theory and experiments will finally be carried out and discussed.

2. Materials and methods

Contact system and 3D imaging. We investigate in this work a sphere-on-plane contact system made of a soft elastomeric hemisphere (deformable body, Young's modulus $E \sim 1.5$ MPa, radius of curvature $R = 9.42$ mm) in contact with a stiff plate made of PMMA (polymethylmethacrylate, $E \sim 3$ GPa). The deformable body has a cylindrical base (diameter $d = 12$ mm) and a total height $h = 6$ mm. It is made of PDMS (Sylgard 184 silicone, Dow Corning) filled with 3 vol% aluminum powder particles of typical size between 16 μm to 24 μm (eConduct Aluminum 202000, Eckart), the latter being solely used as markers in the 3D images to be acquired by XRCT. The smooth spherical contact surface was fabricated using a two-step pouring process of liquid PDMS into a 3D-printed cylindrical mold, in which a smooth concave glass lens was embedded. First, a small droplet of particle-free PDMS was spin-coated onto the lens surface, creating a thin layer (~ 30 μm thick) of pure PDMS. This step ensures that the contact interface remains free from potential alterations caused by the presence of particles. Subsequently, the remaining particle-seeded PDMS was poured into the mold before curing, as [33]. Further details on the sample preparation procedure can be found in Acito et al. [26].

The laboratory tomograph used in this work is a V|TomeX (Phoenix X-ray GmbH) with a 2520 V detector from Varian (1920 × 1536 pixel matrix) and an X-ray source operated at 80 kV and 280 mA. At each contact loading step, 900 radiographs with an exposure time of 999 ms each were taken during the 360° rotation of the specimen. Reconstruction of the 3D volumes was performed with the filtered back-projection algorithm Feldkamp et al. [34] implemented in the software available with the tomograph. The configuration adopted here allows to reach a voxel size of 4 μm.

A new *in situ* tribometer was developed on purpose in this work, with the objective of performing contact experiments under normal loading in the tomograph. Figs. 1.a and 1.b show the details of the system, involving a 3-axis load sensor (2 mN accuracy), a linear translating stage, only used for shear experiment, and two goniometers for alignment, mounted on the upper end of a 30 mm PMMA tube. The latter connects the tribometer to the lower part of a conventional *in situ* tension/compression rig designed for XRCT analysis [35], mounted on the motorized stage of the tomograph. The inset in Fig. 1.b shows a radiograph of the contact system fitted in the *in situ* tribometer. In this work, we focus on a displacement-driven normal contact experiment, where the normal displacement is incrementally increased, resulting in an increase in the normal load P, while the shear displacement — and thus the shear load Q — remains zero. Fig. 1.c shows the loading curve recorded during the test. Each incremental step consists of an initial loading phase, followed by a 5 min relaxation period and a subsequent 20 min XRCT scan. A slight relaxation of the normal load P can be observed during each loading step. Seven loading steps were carried out in total, imposing incremental normal indentation depths δ_c of: 16 μm, 56 μm, 95 μm, 135 μm, 174 μm, 215 μm and 252 μm. The stabilized maximum reaction force on the load cell in the last step was 1.48 N. Due to the long duration of the experiment and the large amount of subsequent analysis, only one test was conducted under these conditions. Therefore, it should be considered a proof of concept, and small changes in the sample formulation, geometry, or loading conditions are expected to produce different responses from the viscoelastic PDMS body. However, it was verified with the present sample on a separate opto-mechanical device [26] that the 5 min relaxation period before scanning was sufficient to stabilize the contact area.

Fig. 2 shows a detailed XRCT view of the contact system. The fine dispersion of white aluminum particles is visible in Fig. 2.a, corresponding to the middle XZ slice in the reconstructed XRCT volume at step 0 (initial state). Fig. 2.b shows the same slice at step 7 (indentation δ_c 252 μm), where the establishment of a contact radius a can be observed, along with the upward movement of individual particles in PDMS. 3D renderings of the PDMS deformable body are depicted in Fig. 2.c (step 0) and Fig. 2.d (step 7).

The application of Digital Volume Correlation (DVC), as used in this work to compute the displacement field from the successively reconstructed volumes, is illustrated in Fig. 3. The analysis employs the global DVC procedure implemented in the open-source software pyFEDIC, developed at INSA Lyon by Lachambre [36]. Fig. 3.a shows the finite element mesh discretizing the region of interest (ROI) within the PDMS body. The selected mesh size of 96 μm — significantly larger than the typical particle size — ensures sufficient contrast from the 3D markers throughout the entire mesh.

The Digital Volume Correlation (DVC) scheme employed here closely follows the approach detailed in Lachambre et al. [30], referred to as "conventional DVC with initialization" in Fig. 7 of [30].

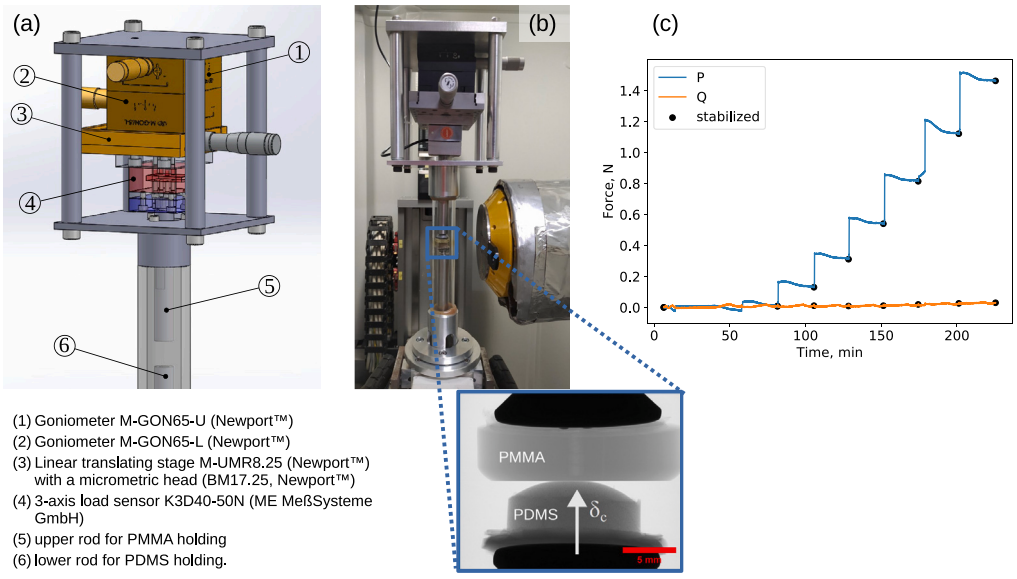

Fig. 1. (a) 3D geometry of the designed XRCT *in situ* tribometer. (b) Picture of the tribometer installed in the tomograph, the inset showing a radiograph of the investigated sphere-on-plane contact system. (c) Loading curves (normal and tangential forces, P and Q) acquired during the *in operando* contact experiment, focusing here on the compression part (no tangential loading of the contact system is imposed).

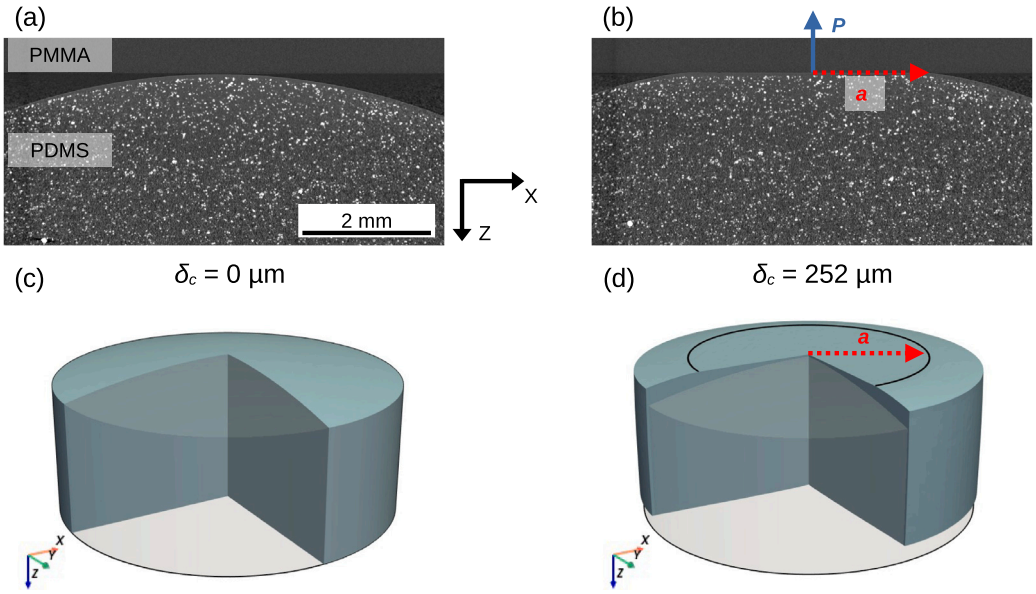

Fig. 2. Slices of the reconstructed volumes in the central XZ plane ($Y = 0$) before (a) and after (b) the application of indentation, $\delta_c = 252$ µm. The red (resp. blue) arrow shows the apparition of a contact area of radius a (resp. normal force P). (c) and (d) depict the corresponding 3D views of the deforming PDMS sample, where the undeformed shape appears in transparency.

In this conventional DVC framework, the displacement field at step i is consistently computed relative to the initial volume at step 0. Note however that the resolution of the displacement field at step i is initialized using results from image correlation performed at two coarser scales, using downsized (binned) volumes. This allows us to calculate a fast approximation of the DVC displacement fields. The first approximation is obtained with a coarse finite element mesh (element size $4\times96 = 384$ µm). It is refined in a second step with an intermediate mesh (element size $2\times96 = 192$ µm), which is finally used to initialize the displacement field in the iterations of the DVC algorithm at the target 96 µm element size. The latter was selected as a compromise between a fine FE discretization of the deforming body and a low uncertainty of the calculated DVC displacement. In this configuration, the uncertainty of the DVC displacement field was estimated to be 0.086 voxels for a prescribed rigid body translation of the sample by one voxel. Further details on the evaluation of DVC uncertainty can be found in Lachambre et al. [30]. The conventional DVC scheme with initialization allows to achieve a rather low level of correlation residuals everywhere in the mesh up to the last deformation step, as illustrated in Figs. 3.c and 3.d. The correlation residuals represent the misfit between the initial image and the deformed image corrected from the computed displacement field. The boxplots in Fig. 3.c demonstrates that the correlation residuals remain consistently below a maximum of $\sim$ 8% of the image dynamics across all compression steps. The 3D rendering of residuals in Fig. 3.d indicates that their maximum is achieved at the bottom and top (contact) surfaces of the PDMS sample.

In this work, no regularization of the mechanical fields was applied during the iterative process of the DVC algorithm to determine the

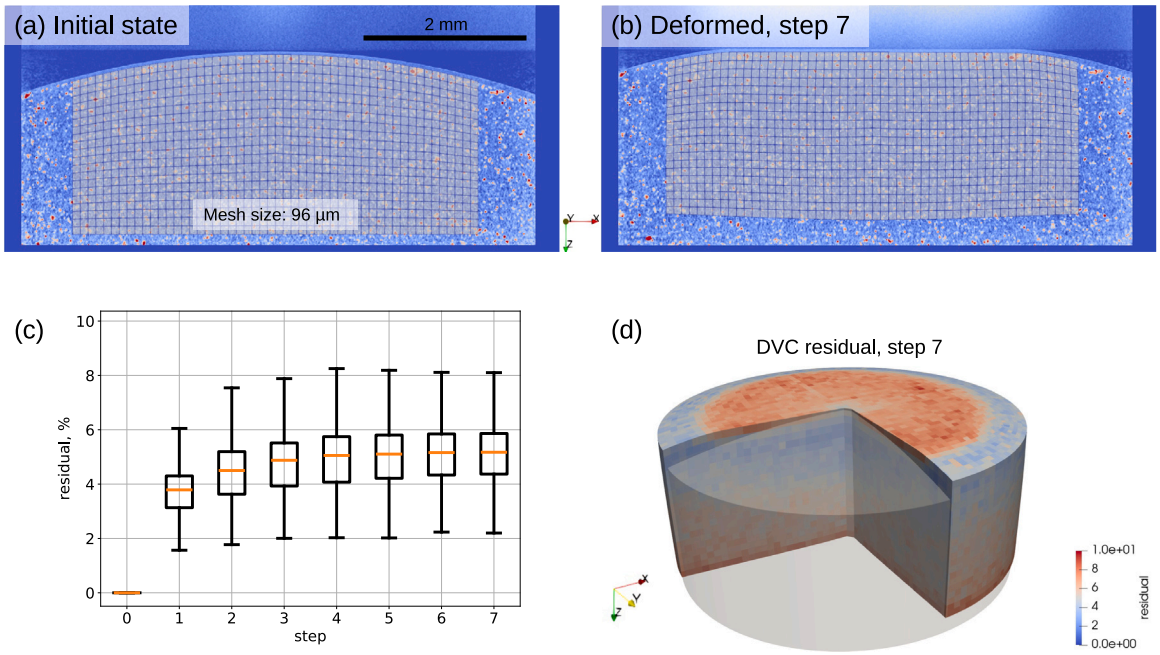

Fig. 3. Digital Volume Correlation and evolution of the investigated region of interest (ROI). (a) Central XZ slice of the initial FE mesh with the underlying markers in the bulk of the PDMS sample. (b) Deformed image and FE mesh at the end of compression (step 7). (c) Boxplot of the evolution of correlation residuals during compression. (d) 3D view of the residual field at step 7 ($\delta_c = 252$ µm) in the bulk of PDMS.

displacement field. As detailed in Réthoré et al. [37] or Mendoza et al. [38], regularization would act as a mechanical filter on the DVC displacement field, assuming a for example a linear elastic constitutive behavior of the material. Since the behavior of PDMS is *a priori* more complex than linear elasticity (namely hyperelastic and viscoelastic) and the contact surface presumably experiences some adhesion, turning off regularization allows us to obtain the most accurate displacement field possible for describing the sample's deformation, regardless of the underlying contact physics or material mechanics. Nevertheless, the displacement field obtained from DVC is smoothed using a median filter during each iteration. In fact, both the overall low level of correlation residuals and the accuracy of the deformed shape in Fig. 3.b — closely matching the deformation flow of the PDMS, including at the contact surface — suggest that the obtained displacement field is realistic.

Establishment of a stress field. The primary objective of this article is to compare theoretical predictions of displacement, strain, and stress fields with experimentally derived fields computed directly from Digital Volume Correlation (DVC) measurements. Particular emphasis is placed on the stress field, without relying on numerical contact algorithms. To evaluate these fields, we consider the three methods detailed in the following. The first one is based on Hertzian theory, while the last two methods are based on DVC measurements.

1. The first method is based on theoretical predictions using the Hamilton elastic model [6] in the particular case where the tangential force is considered zero (and thus the loading is purely normal) and will be referred to as "Hamilton" in the results presented in Section 3. Hamilton's explicit equations for stresses allow us to assess the stress field under the assumption of an equivalent linear elastic material behavior. Notably, these explicit equations are derived for stresses — not displacements or strains — and inherently satisfy the equilibrium equations:

$$\mathrm{div}(\sigma_{ij}) = 0 \tag{1}$$

or equivalently expressed over the tree axes x, y, z:

$$\frac{\partial \sigma_{xx}}{\partial x} + \frac{\partial \sigma_{xy}}{\partial y} + \frac{\partial \sigma_{xz}}{\partial z} = 0 \tag{2}$$

$$\frac{\partial \sigma_{xy}}{\partial x} + \frac{\partial \sigma_{yy}}{\partial y} + \frac{\partial \sigma_{yz}}{\partial z} = 0 \tag{3}$$

$$\frac{\partial \sigma_{xz}}{\partial x} + \frac{\partial \sigma_{yz}}{\partial y} + \frac{\partial \sigma_{zz}}{\partial z} = 0 \tag{4}$$

Here, we evaluated the displacement field corresponding to Hamilton's stress field by computing the integrals of the harmonic stress functions, $\Psi(E, \nu, P, a, x, y, z)$ and $\Omega(E, \nu, P, a, x, y, z)$, from which the displacement field is derived under normal contact conditions. The Python code implementing this approach is available in a GitHub repository [40].
From a practical standpoint, our method involves identifying the equivalent Hertzian material, best fitting the experimental deformed shape of the sample. Specifically, we determine the optimal Young's modulus (E) and Poisson's ratio (ν) to use in the Hamilton prediction in order to minimize the misfit between the experimental and Hamilton's displacement fields at the ROI boundary surfaces (including the contact area). This process is illustrated in Figs. 4.a and 4.b. Considering a range of tentative values of E and ν to use in Hamilton's equations, we define an error function that weights equally: (i) the misfit in contact radius, the magnitude of displacement misfit at the lateral surface (ii), as well as at the bottom surface (iii) and at the top surface (iv) of the ROI. These misfits are normalized by their maximum over the investigated range of E and ν. Fig. 4.b shows the resulting map of the normalized error as a function of E and ν. The optimized configuration, shown in Fig. 4.a, corresponds to $E = 1.55$ MPa and $\nu = 0.49$, where the misfit displacement remains below 32 µm across all boundary surfaces.
2. The second method is based on DVC experimental measurements and will be referred to as "DVC" in the results presented in Section 3. This method consists in directly computing the strain field from the DVC displacement field,

$$\varepsilon_{ij} = \frac{1}{2}\left(\frac{\partial u_i}{\partial x_j} + \frac{\partial u_j}{\partial x_i}\right) \tag{5}$$

and the stress field using Lamé equations for the equivalent linear elastic isotropic material:

$$\sigma_{ii} = \frac{E}{1+\nu}\left(\frac{\nu \Delta}{1-2\nu} + \varepsilon_{ii}\right) \tag{6}$$

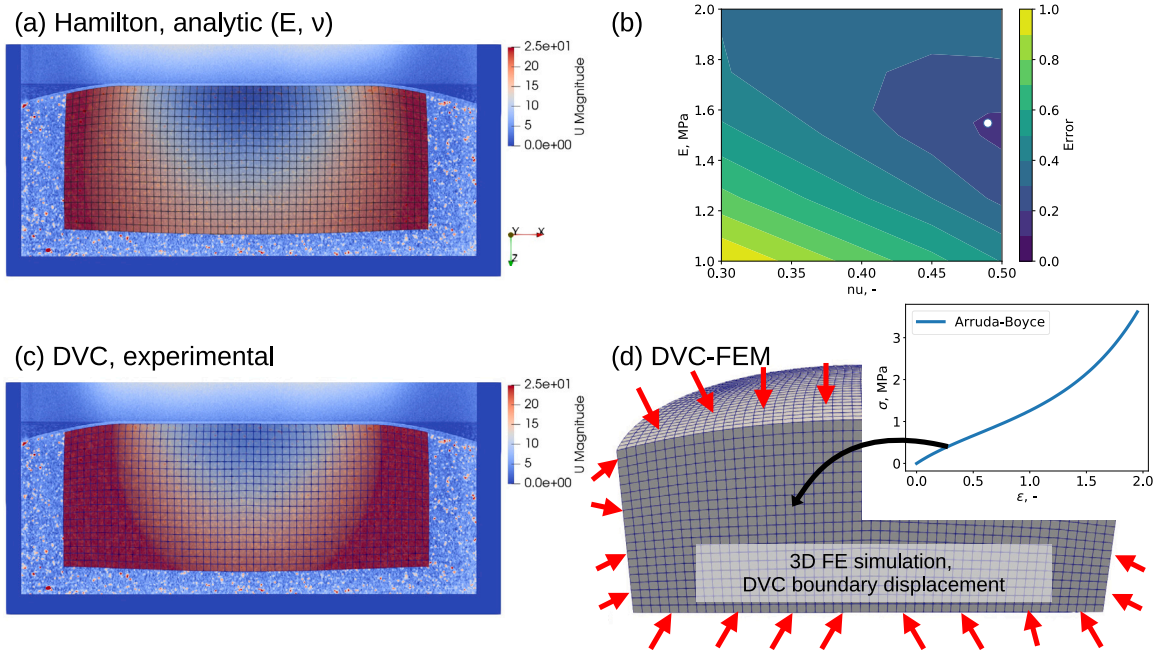

Fig. 4. Establishment of stress fields from XRCT experiments and DVC analysis. (a) Central XZ slice of the deformed XRCT volume at step 7 together with the ROI subjected to the analytical displacement field of Hamilton [6] ($P = 1.48$ N, $Q = 0$ N, $E = 1.55$ MPa, $\nu = 0.49$). (b) Normalized error map of the Hamilton displacement field at the ROI boundary surfaces for a range of Young's moduli and Poisson's ratios. The white point represents the chosen optimum, $E = 1.55$ MPa, $\nu = 0.49$. (c) Experimental DVC displacement field at step 7. (d) Finite Element simulation setup where the ROI mesh is subjected to the DVC displacement field at the boundary surfaces. The constitutive behavior of PDMS is described as an hyperelastic Arruda–Boyce behavior [39] depicted in the inset. The color code in (a) and (c) corresponds to the magnitude of the displacement field.

for normal stresses, with $\Delta = \varepsilon_{xx} + \varepsilon_{yy} + \varepsilon_{zz}$ the dilation, and

$$\sigma_{ij} = \frac{E}{1+\nu}\varepsilon_{ij} \tag{7}$$

for shear stresses. One should point out that this stress field is not guarantied to be at equilibrium ($\mathrm{div}(\sigma_{ij}) = 0$) in the absence of a proper regularization scheme in the DVC algorithm.

3. The third method is also based on DVC experimental measurements and will be referred to as "DVC-FEM" in the results presented in Section 3. This method aims to determine a stress field that ensures stress equilibrium in the deforming material while strictly adhering to the boundary displacements of the ROI's outer surfaces, as measured by DVC. This approach assumes an actual hyperelastic constitutive behavior for PDMS. We chose to transition from purely elastic models (methods 1 and 2) to a hyperelastic model, as the latter is known to better capture the behavior of PDMS [15,41]. To achieve this, we employ finite element (FE) analysis within the Abaqus environment, assuming an Arruda–Boyce hyperelastic behavior where the boundary conditions are fully driven by the DVC surface displacement field. Importantly, no contact assumptions or numerical FE contact parameters are involved in establishing the stress field. Figs. 4.c and 4.d illustrate the experimental displacement field and its application to the boundary surfaces of the mesh in the FE simulation. The Arruda–Boyce (AB) parameters of the present PDMS sample are $\mu = 0.489$ MPa, $\lambda_m = 1.917$ and $D = 0.067\ MPa^{-1}$, the latter corresponding to a ratio of the initial bulk modulus to the initial shear modulus of 50 or equivalently to a 0.49 Poisson's ratio.

Finally, it is possible to perform the full FE simulation of the test using the idealized geometry of the contact system and a FE numerical contact algorithm. Since this is not the main scope of the present paper, we will only briefly discuss this option in the Discussion section. We used in that case the hard contact algorithm of Abaqus, with a 2.0 coefficient of friction and the default penalty friction formulation.

All FE simulations are performed with the implicit solver of Abaqus, using 8-node brick elements, reduced integration and hybrid formulation with constant pressure (C3D8RH). Hybrid formulation helps accounting for the incompressible, non-linear behavior of PDMS. Note that we have checked that the reaction force of the simulated contact system matches the stabilized force of Fig. 1.c at the seven imposed indentation levels with these parameters.

3. Results

Contact area. The first quantity of interest that can be easily determined from the deformed DVC meshes of Fig. 3 is the contact area. The surface profiles of Fig. 5.a show how the hemispherical PDMS surface is being flattened on the PMMA plane in the course of deformation. To capture the evolution of the contact area at each loading steps, we define a threshold of 2 degrees relative to the vertical (Z) axis. This threshold is applied to filter surface elements of the mesh based on the Z-component of their normals (i.e., only elements whose normals deviate by less than 2° from the vertical are retained as belonging to the contact area). The resulting evolution of the contact region throughout the loading process is illustrated in Fig. 5.b. It shows the expected circular shape upon increasing indentation for such sphere-on-plane contact system under normal loading. Fig. 5.c plots the corresponding evolution of contact radius a as a function of the normal load P. One can see that the contact radius determined by XRCT and DVC follows rather closely the evolution of the one predicted by the Hertzian theory (orange dashed line), simplifying in the present case to:

$$a_H = \left(\frac{3PR(1-\nu^2)}{4E}\right)^{1/3} \tag{8}$$

where $R = 9.42$ mm, and we use the optimized values $E = 1.55$ MPa and $\nu = 0.49$ obtained from the "Hamilton" method, as detailed in the previous section. The blue curve in Fig. 5.c shows an additional confirmation of the evolution of contact radius as measured separately (on the same sample) using an optomechanical device looking at the contact surface

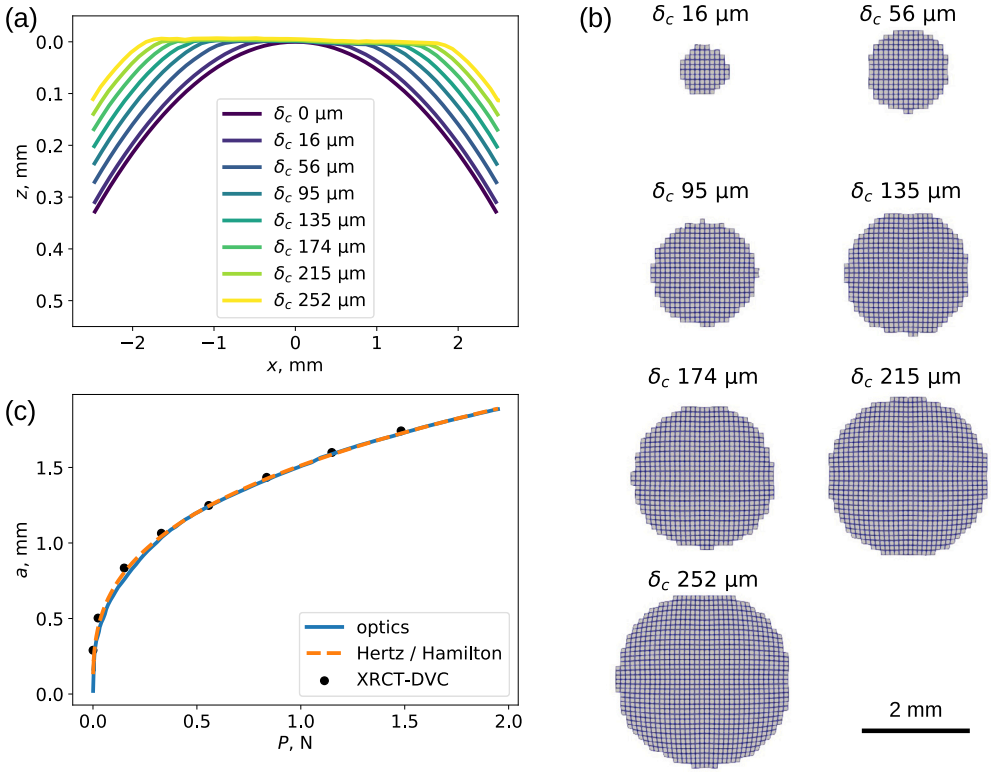

Fig. 5. Determination of contact radius from the DVC deformed surface. (a) PDMS surface profile in the central XZ plane at increasing indentation δ_c. (b) Contact area extracted from the DVC deformed meshes. (c) Evolution of the determined contact radius (black disks) as a function of normal load, compared to the reference optomechanical experiment [26] (blue solid line) and to the prediction of Hertz theory with $R = 9.42$ mm, $E = 1.55$ MPa and $\nu = 0.49$ (orange dashed line).

from the top. This device and the corresponding experimental protocol is described in details in Lengiewicz et al. [15] and Acito et al. [26].

It is worth noting that the current procedure for determining the contact radius, a, — based on X-ray computed tomography (XRCT) and deformed surfaces obtained via Digital Volume Correlation (DVC) — effectively addresses many of the challenges highlighted by Acito et al. [26]. Specifically, this approach mitigates the tendency to overestimate the contact area when using 3D images with finite voxel resolution. This improvement stems from the higher accuracy of the DVC displacement field, which is finer than the voxel size (as demonstrated by Lachambre et al. [30] for a similar experimental setup). Unlike traditional methods, our procedure does not rely on image segmentation or marching cube algorithms for surface extraction, thereby avoiding associated inaccuracies.

Displacement field. Fig. 6 shows the normalized displacement field (U_i/δ_c) beneath contact in the middle XZ plane of the PDMS sample at step 7, i.e. 252 µm indentation. The experimental DVC fields of Figs. 6.a (U_y/δ_c), 6.b (U_z/δ_c) and 6.c (U_x/δ_c) can be compared to the ones obtained with the DVC-FEM procedure (Figs. 6.d, 6.e and 6.f) and with the Hamilton model (Figs. 6.g, 6.h and 6.i). DVC, DVC-FEM and Hamilton displacement fields look rather similar, both qualitatively and quantitatively, for the three components of the displacement. For a better comparison, the color map of each column in the figure is identical. U_x component shows an antisymmetric distribution reversing at $x = 0$, with an absolute maximum around $x = a$ and $z = 0.5a$. The antisymmetry observed in the middle XZ plane arises from the axisymmetric geometry of the sample and the axisymmetric loading conditions about the Z axis. U_y is close to zero everywhere in the middle XZ plane as expected by the axisymmetry. U_z exhibits the same axisymmetry, with an absolute maximum around 90% of δ_c at the lateral surfaces of the ROI.

Strain field. The strain fields, as derived from the displacement fields of Fig. 6 at step 7 using the three methods presented in Section 2, are illustrated in Fig. 7. Figs. 7.a, 7.b and 7.c depict the three main components of the strain tensor obtained by DVC in the middle XZ plane, namely ε_{xx}, ε_{xz} and ε_{zz}. They can easily be compared to the strain fields obtained with the DVC-FEM method (Figs. 7.d, 7.e and 7.f) and to the ones derived from the equations of Hamilton (Figs. 7.g, 7.h and 7.i). Again the colormaps are identical for a given column in this figure. It is noteworthy that the strain fields obtained from DVC and DVC-FEM exhibit good agreement with the axisymmetry of the sample and loading conditions, which are inherently reflected in the analytical fields derived from the Hamilton model. This gives us confidence in the global alignment of the *in situ* setup and in the DVC displacement fields from which these strain fields are computed.

The DVC, DVC-FEM, and Hamilton analytical fields exhibit strong qualitative similarities, although local variations in the intensity of the strain components are observed. ε_{zz} shows a compressive strain beneath contact, close to -0.10 around $\{x = 0, z = 0.5a\}$ and slightly positive at the surface, outside of the contact area. The compressive ε_{zz} is counter-balanced by tensile ε_{xx} beneath contact ($|x| < a$), which becomes slightly compressive for $|x| > a$ as a response of the surrounding bulk. Indeed, lateral and bottom surfaces are not free surfaces, as opposed to the top surface outside of contact area. ε_{xz} is antisymmetric with an absolute maximum close to $|x| = a$ beneath the surface. Computing the trace of the DVC strain tensor field yields a median volume variation $\Delta V/V$ of 0.2% in the elements, and globally less than 1%. Such low variation of volume is in agreement with the expected nearly incompressible behavior of PDMS.

Stress field. The displacement and strain fields beneath the contact, now accessible through DVC (as illustrated above), enable us to explore various experimentally-driven assessments of the stress field. In Fig. 8, we present the invariants of the stress tensor for the three methods

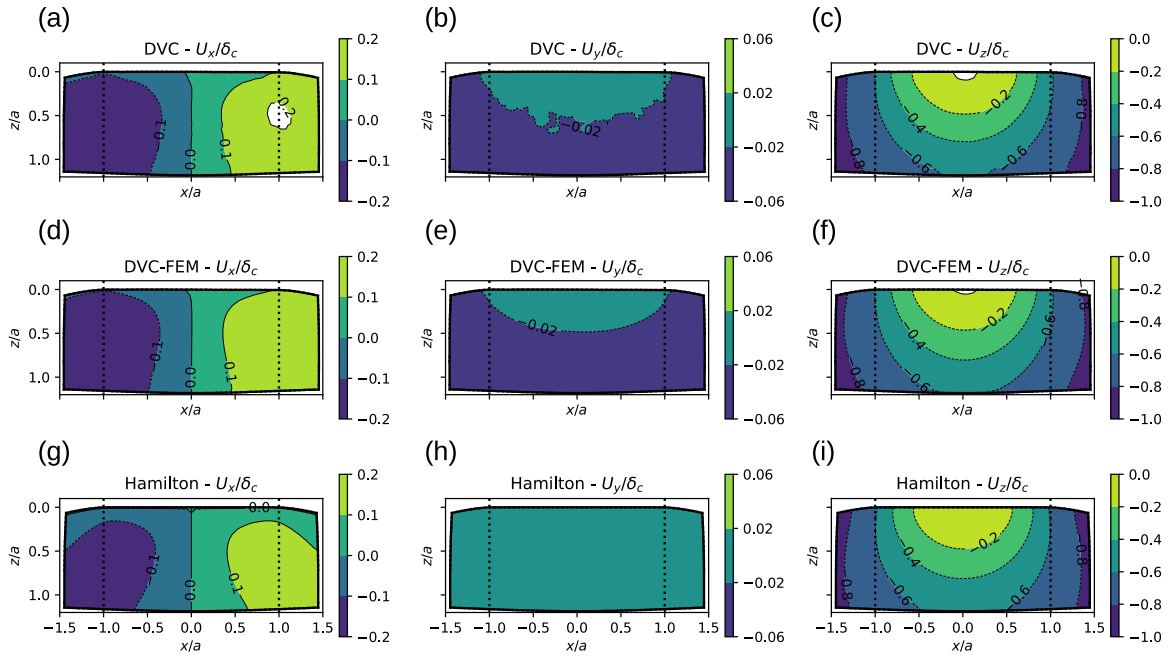

Fig. 6. Normalized displacement field in the bulk of the deforming PDMS sample at step 7 ($\delta_c = 252$ µm, $P = 1.48$ N), in the XZ central plane. (a)–(c) Experimental DVC fields. (d)–(f) DVC-FEM fields. (g)–(i) Hamilton's analytical fields ($R = 9.42$ mm, $E = 1.55$ MPa, $\nu = 0.49$). (a), (d), (g): U_x/δ_c component. (b), (e), (h): U_y/δ_c component. (c), (f), (i): U_z/δ_c component.

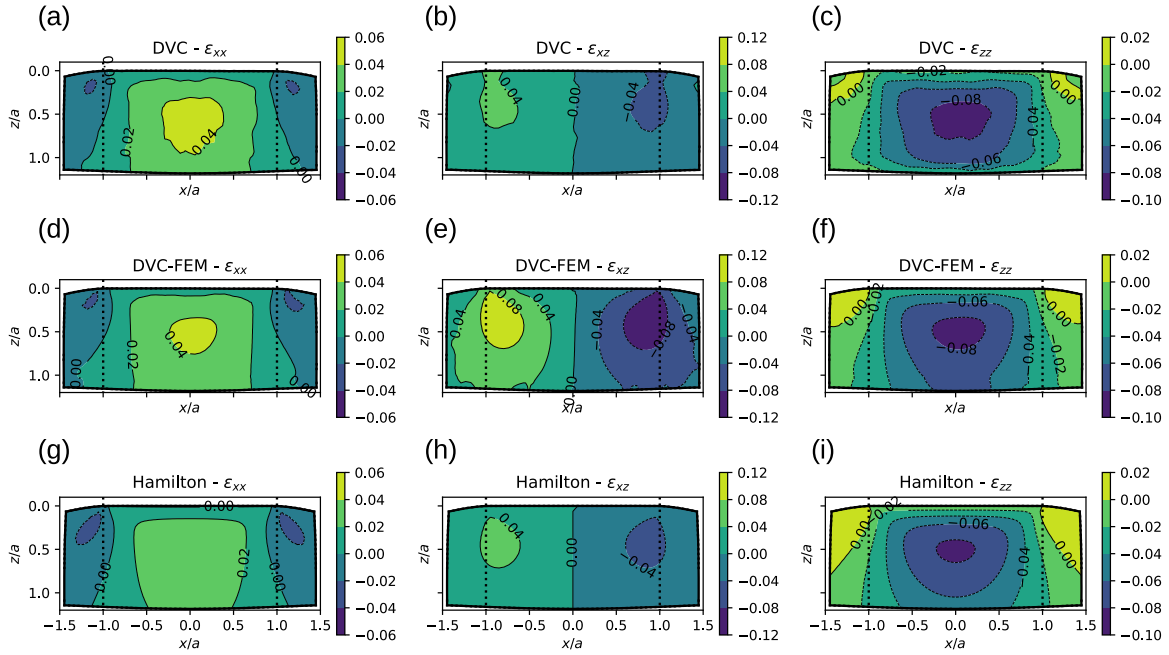

Fig. 7. Strain field in the bulk of the deforming PDMS sample at step 7 ($\delta_c = 252$ µm, $P = 1.48$ N), in the XZ central plane. (a)–(c) Experimental DVC fields. (d)–(f) DVC-FEM fields. (g)–(i) Hamilton's analytical fields ($R = 9.42$ mm, $E = 1.55$ MPa, $\nu = 0.49$). (a), (d), (g): ε_{xx} component. (b), (e), (h): ε_{xz} component. (c), (f), (i): ε_{zz} component.

described in Section 2. For clarity, all stress values are normalized by the maximum pressure at the center of the contact predicted by Hertz theory:

$$p_0 = \frac{3P}{2\pi a^2} \tag{9}$$

Shear stresses are represented in Fig. 8 by the normalized Mises parameter $\sqrt{J_2}/p_0$, where J_2 is the second invariant of the deviatoric stress tensor. The pressure field is represented by the opposite of the mean stress normalized by p_0, $-\sigma_{ii}/(3p_0)$.

Figs. 8.a, 8.d and 8.g show that the normalized Mises stress is qualitatively similar between DVC, DVC-FEM and Hamilton models with a maximum of up to $0.36p_0$ around $\{x = 0, z = 0.5a\}$ in the deformed configuration. Here, to our knowledge, we observe for the first time in three dimension the classical result in tribology, which states that the maximum shear stress occurs beneath the surface at $z = 0.5a$. This specific location is widely recognized as the most favorable point for the initiation of plasticity under contact loading. However, in the case of PDMS, whose behavior remains purely elastic, this observation is of

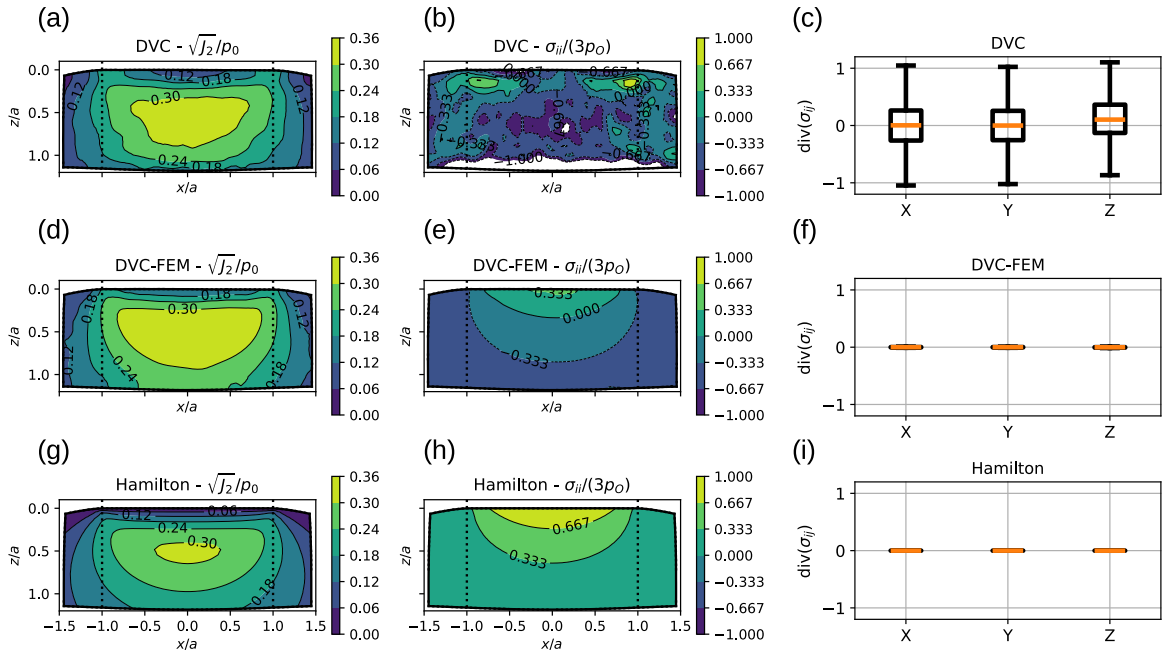

Fig. 8. Normalized stress fields in the bulk of the deforming PDMS sample at step 7 (δ_c = 252 μm, P = 1.48 N), in the XZ central plane. All stresses are normalized by the Hertzian maximum contact pressure p_0 = 0.238 MPa. (a)–(c) Experimental DVC fields. (d)–(f) DVC-FEM fields. (g)–(i) Hamilton's analytical fields (R = 9.42 mm, E = 1.55 MPa, ν = 0.49). (a), (d), (g): Normalized Mises parameter $\sqrt{J_2}/p_0$. (b), (e), (h): Normalized pressure $-\sigma_{ii}/(3p_0)$. (c), (f), (i): Boxplots of the divergence of the stress field over the X, Y and Z directions.

course not directly relevant. The normalized pressure is however quite different between the models in Figs. 8.b, 8.e and 8.h. Hamilton's pressure field (Fig. 8.h) reaches p_0 in the center of contact area (Hertzian distribution) and is positive (compressive) everywhere in the bulk. The DVC-FEM pressure field (Fig. 8.e) exhibits a distribution similar to that predicted by the Hamilton model. However, it displays an *a priori* unrealistic shift toward tension (i.e., negative pressure) outside the immediate vicinity of the contact region. Further discussion on this observation is provided in Section 4. The direct elastic stress, derived from the DVC strain field (Fig. 8.b), exhibits significant scattering, with local minima and maxima approaching $\pm p_0$. Numerical computation of the divergence of stress fields over the $\{X, Y, Z\}$ axes confirms that the DVC stress field is not at equilibrium in the bulk of PDMS (Fig. 8.c), while the two others are (Figs. 8.f and h).

4. Discussion

The *in situ* X-ray computed tomography (XRCT) setup presented in this work enables, for the first time, the experimental assessment of the 3D stress field beneath a contact using the displacement field provided by Digital Volume Correlation (DVC). Unlike recent studies in the field of photoelasticity (e.g., Mitchell et al. [32]), it is important to highlight that XRCT and DVC techniques do not require any *a priori* assumptions regarding the nature of the mechanical fields, such as plane-stress or axisymmetry, although the contact system investigated here does exhibit axisymmetry due to purely normal loading. The ability to acquire these fields in 3D, *in situ*, and non-destructively opens new perspectives and challenges in the field of contact mechanics. Specifically, it is now possible to explicitly compare and evaluate the validity of pioneering theories, such as those proposed by Hertz [1], Huber [2] or Hamilton [5,6], against the corresponding full-field experimental data. Additionally, the availability of experimental 3D data will facilitate the evaluation of different formulations of numerical contact algorithms, which are widely used in finite element (FE) simulations. However, this topic is beyond the scope of the present paper.

While this paper does not aim to draw conclusions regarding the adequacy or inadequacy of Hertzian theories in representing our 3D experimental data, the systematic comparison of all forms of these fields — from displacements to strain and stress fields — has revealed several key observations, which are discussed below.

Direct comparison of displacement, strain or stresses. Widely used image correlation techniques in modern experimental mechanics provide direct access to displacement fields (from which strain fields can be derived), but not to stresses. This contrasts with many mechanical theories, such as the Hertz or Hamilton equations (considered here for pure normal loading), which are originally formulated in terms of stress fields. Consequently, comparing theoretical predictions with experimental results is challenging, as it requires postulating a constitutive behavior to convert displacement and strain fields into stresses. To address this issue, we computed the underlying displacement field associated with Hamilton's equations [40]. This approach may serve as a valuable tool for future research aiming to establish a direct dialogue between experiments and Hertzian contact theories for linear elastic solids. Additionally, this paper adopts a complementary approach by using a finite element (FE) solver to compute the equilibrated stress field within the bulk of the deforming sample. This method incorporates the Arruda–Boyce hyperelastic constitutive behavior of PDMS, combined with the experimentally measured boundary surface displacements obtained via DVC.

Figs. 6 (displacement), 7 (strain) and 8 (stress) depict an increasing discrepancy between the different methods to assess the mechanical fields beneath contact. Stress fields, which are experimentally difficult to access, appear here to be most discriminant when it comes to the decision on whether or not measured mechanical fields are likely to be realistic (or admissible) ones.

The differences between the methods used to assess the stress fields are further detailed in Fig. 9, which presents stress profiles at the contact surface ($y = z = 0$) or at the vertical below the contact center ($x = y = 0$). Hamilton's profiles (green lines) confirm the parabolic, Hertzian distribution of the normalized pressure, $-\sigma_{ii}/(3p_0)$, at the contact surface (see Fig. 9.a), while the normalized Mises parameter, $\sqrt{J_2}/p_0$, remains close to zero (see Fig. 9.b). The DVC-FEM profiles (orange lines) exhibit a distribution similar to Hamilton's, but with a shift

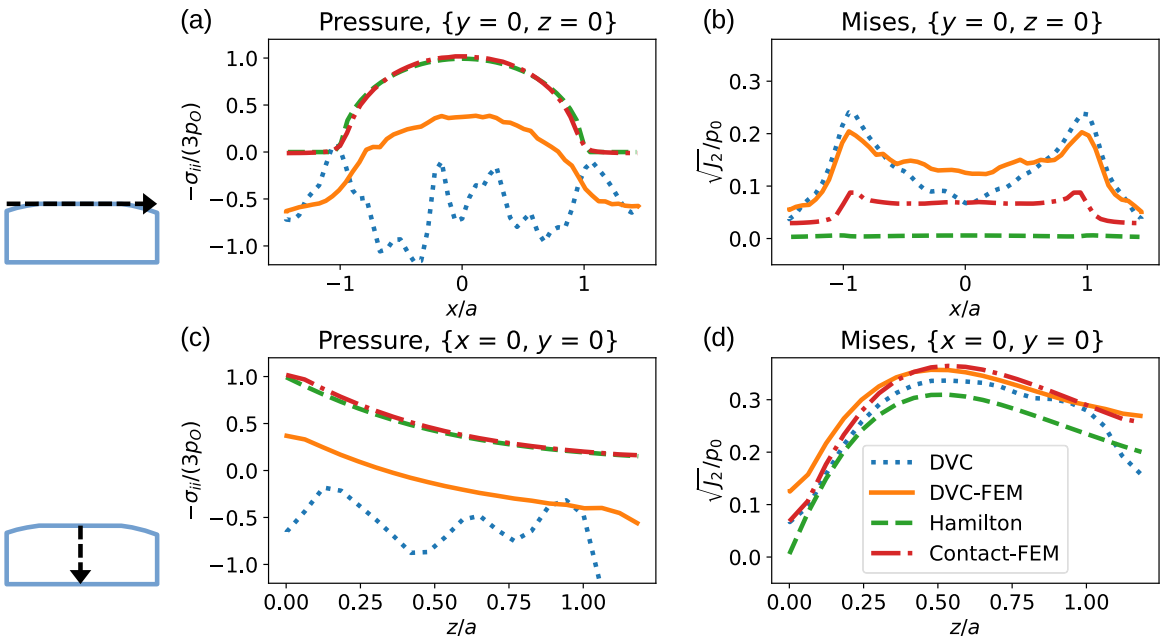

Fig. 9. Stress profiles at step 7 (δ_c = 252 µm, P = 1.48 N), in the XZ central plane. All stresses are normalized by the Hertzian maximum contact pressure p_0 = 0.238 MPa. (a) Normalized pressure $-\sigma_{ii}/(3p_0)$ and (b) normalized Mises parameter $\sqrt{J_2}/p_0$ at the contact surface ($y = z = 0$). (c) Normalized pressure $-\sigma_{ii}/(3p_0)$ and (d) normalized Mises parameter $\sqrt{J_2}/p_0$ beneath the contact center ($x = y = 0$). Colors refer to different calculations, see legend on panel (d).

toward tensile stresses outside the contact radius for the pressure and an amplification of the Mises parameter. Notably, the DVC-FEM Mises parameter is non-zero within the contact area. The unequilibrated DVC stress field (blue lines), particularly for the pressure distribution, shows an erratic evolution in the contact region. This confirms that, despite being the most direct and simplest method, it is far from the most appropriate for deriving the stress field. Figs. 9.c and 9.d illustrate the respective evolutions of pressure and Mises parameter, along the vertical axis passing through the contact center. All curves (except for the DVC method) exhibit expected qualitative trends, though without quantitative agreement. In Fig. 9.d, the maximum shear stress is again observed beneath the contact at approximately 0.5 times the contact radius inside the bulk of the PDMS. The final profiles in Fig. 9 correspond to the contact FEM case (red lines), using the Abaqus hard contact algorithm with a friction coefficient of 2.0 and the full geometry of the PDMS sample (diameter d = 12 mm, height h = 6 mm, radius of curvature R = 9.42 mm) in contact with an analytical rigid PMMA plane. These profiles show a global evolution similar to Hamilton's for the pressure distribution within the contact area, but with slight shifts or amplifications for the Mises parameter. In this case, the shear stress is non-zero within the contact area, and all stress components vanish at the free surface outside the contact area.

Identifying the exact origin of the quantitative discrepancies observed between the theoretical models and the experimentally derived DVC stress fields is beyond the scope of this paper. However, it is evident that none of the models used — whether for measurements or comparisons — are sufficiently sophisticated to fully capture the behavior of PDMS. PDMS is a viscoelastic, highly adhesive, and highly frictional material, which does not align with the assumptions of Hamilton's calculations (purely elastic material with no adhesion or friction) or our FEM simulations (hyperelastic material with no adhesion). Additionally, PDMS is nearly incompressible, leading to convergence issues in FEM computations and to direct stress components σ_{ii} that are extremely sensitive to potential local fluctuations of the dilation Δ, as highlighted in Eq. (6) (Section 2) in the linear elastic case with the denominator approaching zero as ν tends towards 0.5. This is a problem near the surface where the DVC residuals are maximal, added to the potential effect of adhesion on the stress state close to the surface. Adhesion would indeed promote the development of tensile stresses at contact surface. To enable a quantitative comparison between experiments and models in future work, more complex models or materials with simpler mechanical behaviors may be required.

Finally, it is striking to observe how different assumptions regarding boundary conditions and material constitutive behavior can produce similar deformed shapes of the contact sample, yet result in markedly different stress distributions within the bulk. This underscores the ill-posed nature of image correlation techniques, where multiple displacement fields may yield comparable levels of correlation residuals — and thus similar accuracy in describing material deformation — while corresponding to distinct mechanical states. This highlights the well-known challenge of mechanical regularization in image correlation, which we address below.

DVC regularization. In this study, we deliberately chose not to apply any mechanical regularization during the image correlation process. This decision allowed the DVC algorithm to determine a displacement field that best matches the deformation of the internal speckle pattern (aluminum particles) within the PDMS under loading. As shown in Fig. 3, the deformed DVC mesh closely follows the deformation of the PDMS throughout the region of interest (ROI), including in the vicinity of the contact. The corresponding correlation residuals remain globally very low, with a median value of the order of 5 %. However, the stress field, computed under the assumption of a linear elastic equivalent material, is not in equilibrium, as illustrated in Fig. 8.c. Additionally, the correlation residuals are locally higher at the contact surface, as seen in Fig. 3.d. Recent advancements in DVC regularization schemes could address these issues by achieving a better balance between mechanically admissible displacement fields and the accuracy of sample deformation. For instance, the "complete regularization" scheme proposed by Mendoza et al. (2019) [38] was specifically designed to incorporate surface boundary conditions (either Dirichlet or Neumann type) during DVC regularization, in addition to bulk equilibrium constraints. This approach is not presently implemented in the pyFEDIC software used in this work (Lachambre [36]). It is nevertheless likely to improve both the convergence of the DVC algorithm and the level of correlation residuals, particularly at the contact surface, where the evolving contact boundary conditions are challenging to handle using standard bulk regularization techniques.

Towards time resolved experiments. Beyond the challenge of obtaining an admissible experimental displacement field for comparison with contact theories lies the question of selecting a reasonable constitutive behavior assumption for the deforming material. The model contact system studied here employs a PDMS elastomer, with a Young modulus in the order of 1.5 MPa. This choice was motivated by the need to establish a large contact area at low force, easily observable under in situ X-ray computed tomography (XRCT). However, the loading curves in Fig. 1.c reveal significant stress relaxation, as expected for such a viscoelastic elastomeric material tested at room temperature (well into its rubbery state). To mitigate this effect, we implemented a 5 min dwell time before each tomography scan in Section 2, ensuring that no noticeable sample movement occurred during the ~20 min scanning time. This relaxation provides clear evidence of the material's viscoelasticity, in addition to its hyperelastic behavior at finite strain. Given the relatively long scanning time associated with our lab-based tomograph, the present experimental setup primarily captures the quasi-static response of the contact system. Nevertheless, it remains unclear how stress relaxation during the dwell and scanning times affects the measured displacement field and the inferred stress fields, whether assuming an equivalent linear elastic behavior or an actual hyperelastic strain energy potential. Previous work by Yoneyama et al. (1998) [31] demonstrated such stress relaxation beneath contact in polyurethane rubber using photoviscoelasticity. A promising avenue for future research would be to conduct similar in situ contact experiments using a synchrotron X-ray source, which would allow for much faster acquisition rates. This would allow us to move from the so called "interrupted in situ" loading mode used in the present study, to a "continuous in situ" loading mode (see Maire et al. [42] for more details). To achieve this, the displacement during the acquisition of one scan should be smaller than a pixel. This approach would enable the experimental quantification of viscoelasticity's contribution to the establishment of the relaxed stress field beneath the contact.

5. Conclusions

In this work, we presented a novel experimental setup that enables 3D, full-field, and non-destructive access to the mechanical fields beneath a contact. This setup was applied to a model sphere-on-plane contact system subjected to compressive loading. By using a PDMS elastomer embedded with aluminum particles, we created a 3D internal speckle pattern within the deforming body. This pattern was easily tracked using laboratory X-ray computed tomography (XRCT) and analyzed through digital volume correlation (DVC). We proposed multiple strategies to assess the 3D stress field beneath the contact, without relying on numerical contact models or their associated assumptions and parameters. This approach allows for direct and explicit comparisons between the experimental fields and the corresponding Hertzian fields. Our results demonstrate that comparing stress fields between experiments and Hertzian theory is more discriminative than comparing strain or displacement fields. However, this will require in the future the use of more sophisticated models that account for the global behavior of the specimen, including elasticity, adhesion, friction, and other factors. This work highlights the need for adapted regularization schemes in DVC algorithms, which should properly incorporate evolving contact boundary conditions to identify an admissible experimental displacement field. Future perspectives for this experimental setup include sheared contact experiments and time-resolved in situ tomography. These advancements will help clarify the contribution of viscoelastic relaxation to the 3D contact fields observed in this study.

CRediT authorship contribution statement

Sylvain Dancette: Writing – original draft, Visualization, Validation, Supervision, Software, Methodology, Funding acquisition, Data curation, Conceptualization. **Vito Acito:** Writing – original draft, Methodology, Investigation, Data curation, Conceptualization. **Jérome Adrien:** Writing – review & editing, Methodology, Investigation. **Joël Lachambre:** Writing – review & editing, Software, Methodology. **Eric Maire:** Writing – review & editing, Methodology, Conceptualization. **Julien Scheibert:** Writing – review & editing, Supervision, Methodology, Conceptualization. **Davy Dalmas:** Writing – review & editing, Validation, Supervision, Resources, Project administration, Methodology, Funding acquisition, Conceptualization.

Declaration of competing interest

The authors declare that they have no known competing financial interests or personal relationships that could have appeared to influence the work reported in this paper.

Acknowledgment

This work was supported by the LABEX MANUTECH-SISE (ANR10-LABX-0075) of Université de Lyon, within the Plan France 2030 operated by the French National Research Agency (ANR).

References

[1] H. Hertz, Über die Berührung fester elastischer Körper, J. für die reine und angewandte Math. 92 (1882) 156–171.
[2] M. Huber, On the theory of elastic solid contact, Annln der Phys. 14 (1904) 153–163.
[3] C. Cattaneo, Sul contatto di due corpi elastici. Accademia dei Lincei, Sul contatto di due corpi elastici. Accad. dei Lincei 27 (1938) 342–348.
[4] R.D. Mindlin, Compliance of elastic bodies in contact, J. Appl. Mech. 16 (3) (1949) 259–268, http://dx.doi.org/10.1115/1.4009973.
[5] G.M. Hamilton, L.E. Goodman, The stress field created by a circular sliding contact, J. Appl. Mech. 33 (2) (1966) 371–376, http://dx.doi.org/10.1115/1.3625051.
[6] G.M. Hamilton, Explicit equations for the stresses beneath a sliding spherical contact, Proc. Inst. Mech. Eng. Part C: J. Mech. Eng. Sci. 197 (1) (1983) 53–59, http://dx.doi.org/10.1243/PIME_PROC_1983_197_076_02.
[7] K.L. Johnson, K. Kendall, A.D. Roberts, D. Tabor, Surface energy and the contact of elastic solids, Proc. R. Soc. A 324 (1558) (1971) 301–313, http://dx.doi.org/10.1098/rspa.1971.0141, Publisher: Royal Society.
[8] B.V. Derjaguin, V.M. Muller, Y.P. Toporov, Effect of contact deformations on the adhesion of particles, J. Colloid Interface Sci. 53 (2) (1975) 314–326, http://dx.doi.org/10.1016/0021-9797(75)90018-1.
[9] D. Maugis, Contact, Adhesion and Rupture of Elastic Solids, Springer Science & Business Media, 2000, Google-Books-ID: _UCzUVBuR_oC.
[10] M.H. Müser, W.B. Dapp, R. Bugnicourt, P. Sainsot, N. Lesaffre, T.A. Lubrecht, B.N.J. Persson, K. Harris, A. Bennett, K. Schulze, S. Rohde, P. Ifju, W.G. Sawyer, T. Angelini, H. Ashtari Esfahani, M. Kadkhodaei, S. Akbarzadeh, J.-J. Wu, G. Vorlaufer, A. Vernes, S. Solhjoo, A.I. Vakis, R.L. Jackson, Y. Xu, J. Streator, A. Rostami, D. Dini, S. Medina, G. Carbone, F. Bottiglione, L. Afferrante, J. Monti, L. Pastewka, M.O. Robbins, J.A. Greenwood, Meeting the contact-mechanics challenge, Tribol. Lett. 65 (4) (2017) 118, http://dx.doi.org/10.1007/s11249-017-0900-2.
[11] A.I. Vakis, V.A. Yastrebov, J. Scheibert, L. Nicola, D. Dini, C. Minfray, A. Almqvist, M. Paggi, S. Lee, G. Limbert, J.F. Molinari, G. Anciaux, R. Aghababaei, S. Echeverri Restrepo, A. Papangelo, A. Cammarata, P. Nicolini, C. Putignano, G. Carbone, S. Stupkiewicz, J. Lengiewicz, G. Costagliola, F. Bosia, R. Guarino, N.M. Pugno, M.H. Müser, M. Ciavarella, Modeling and simulation in tribology across scales: An overview, Tribol. Int. 125 (2018) 169–199, http://dx.doi.org/10.1016/j.triboint.2018.02.005.
[12] J.H. Dieterich, B.D. Kilgore, Direct observation of frictional contacts: New insights for state-dependent properties, Pure Appl. Geophys. 143 (1) (1994) 283–302, http://dx.doi.org/10.1007/BF00874332.
[13] R. Sahli, G. Pallares, A. Papangelo, M. Ciavarella, C. Ducottet, N. Ponthus, J. Scheibert, Shear-induced anisotropy in rough elastomer contact, Phys. Rev. Lett. 122 (21) (2019) 214301, http://dx.doi.org/10.1103/PhysRevLett.122.214301, Publisher: American Physical Society.
[14] V. Acito, M. Ciavarella, A.M. Prevost, A. Chateauminois, Adhesive contact of model randomly rough rubber surfaces, Tribol. Lett. 67 (2) (2019) 54, http://dx.doi.org/10.1007/s11249-019-1164-9.
[15] J. Lengiewicz, M. de Souza, M. Lahmar, C. Courbon, D. Dalmas, S. Stupkiewicz, J. Scheibert, Finite deformations govern the anisotropic shear-induced area reduction of soft elastic contacts, J. Mech. Phys. Solids 143 (2020) 104056, http://dx.doi.org/10.1016/j.jmps.2020.104056.

[16] B. Zhang, M. de Souza, D.M. Mulvihill, D. Dalmas, J. Scheibert, Y. Xu, Non-monotonic evolution of contact area in soft contacts during incipient torsional loading, Tribol. Lett. 72 (4) (2024) 132, http://dx.doi.org/10.1007/s11249-024-01930-9.

[17] A. Prevost, J. Scheibert, G. Debrégeas, Probing the micromechanics of a multi-contact interface at the onset of frictional sliding, Eur. Phys. J. E 36 (2) (2013) 17, http://dx.doi.org/10.1140/epje/i2013-13017-0.

[18] A.J. Tuononen, Digital image correlation to analyse stick–slip behaviour of tyre tread block, Tribol. Int. 69 (2014) 70–76, http://dx.doi.org/10.1016/j.triboint.2013.09.003.

[19] A. Chateauminois, C. Fretigny, Local friction at a sliding interface between an elastomer and a rigid spherical probe, Eur. Phys. J. E 27 (2) (2008) 221–227, http://dx.doi.org/10.1140/epje/i2008-10376-5.

[20] A. Chateauminois, C. Fretigny, L. Olanier, Friction and shear fracture of an adhesive contact under torsion, Phys. Rev. E 81 (2) (2010) 026106, http://dx.doi.org/10.1103/PhysRevE.81.026106, Publisher: American Physical Society.

[21] E. Maire, P.J. Withers, Quantitative X-ray tomography, Int. Mater. Rev. 59 (1) (2014) 1–43, http://dx.doi.org/10.1179/1743280413Y.0000000023.

[22] P.J. Withers, C. Bouman, S. Carmignato, V. Cnudde, D. Grimaldi, C.K. Hagen, E. Maire, M. Manley, A. Du Plessis, S.R. Stock, X-ray computed tomography, Nat. Rev. Methods Prim. 1 (1) (2021) 1–21, http://dx.doi.org/10.1038/s43586-021-00015-4, Number: 1 Publisher: Nature Publishing Group.

[23] A. Kriston, T. Fülöp, N.A. Isitman, O. Kotecký, A.J. Tuononen, A novel method for contact analysis of rubber and various surfaces using micro-computerized-tomography, Polym. Test. 53 (2016) 132–142, http://dx.doi.org/10.1016/j.polymertesting.2016.05.019.

[24] F. Zhang, J. Liu, X. Ding, R. Wang, Experimental and finite element analyses of contact behaviors between non-transparent rough surfaces, J. Mech. Phys. Solids 126 (2019) 87–100, http://dx.doi.org/10.1016/j.jmps.2019.02.004.

[25] F. Zhang, J. Liu, X. Ding, Z. Yang, A discussion on the capability of X-ray computed tomography for contact mechanics investigations, Tribol. Int. 145 (2020) 106167, http://dx.doi.org/10.1016/j.triboint.2020.106167.

[26] V. Acito, S. Dancette, J. Scheibert, C. Oliver, J. Adrien, E. Maire, D. Dalmas, On the use of in situ X-ray computed tomography for soft contact mechanics, Eur. J. Mech. A Solids 101 (2023) 105057, http://dx.doi.org/10.1016/j.euromechsol.2023.105057.

[27] D. Maugis, Adhesion of spheres: The JKR-DMT transition using a dugdale model, J. Colloid Interface Sci. 150 (1) (1992) 243–269, http://dx.doi.org/10.1016/0021-9797(92)90285-T.

[28] E. Barthel, Adhesive elastic contacts: JKR and more, J. Phys. D: Appl. Phys. 41 (16) (2008) 163001, http://dx.doi.org/10.1088/0022-3727/41/16/163001.

[29] M.A. Sutton, Computer vision-based, noncontacting deformation measurements in mechanics: A generational transformation, Appl. Mech. Rev. 65 (050802) (2013) http://dx.doi.org/10.1115/1.4024984.

[30] J. Lachambre, A. Sibellas, J. Adrien, J. Papillon, R. Bruant, G. Maurel, E. Maire, Experimental method for rubber deformation analysis using in situ X-ray tomography and digital volume correlation with FEM validation, Tomogr. Mater. Struct. 7 (2025) 100045, http://dx.doi.org/10.1016/j.tmater.2024.100045.

[31] S. Yoneyama, J. Gotoh, M. Takashi, Tricolor photoviscoelastic technique and its application to moving contact, Exp. Mech. 38 (3) (1998) 211–217, http://dx.doi.org/10.1007/BF02325745.

[32] B. Mitchell, Y. Yokoyama, A. Nassiri, Y. Tagawa, Y.P. Korkolis, B.L. Kinsey, An investigation of Hertzian contact in soft materials using photoelastic tomography, J. Mech. Phys. Solids 171 (2023) 105164, http://dx.doi.org/10.1016/j.jmps.2022.105164.

[33] E. Delplanque, A. Aymard, D. Dalmas, J. Scheibert, Solving curing-protocol-dependent shape errors in PDMS replication, J. Micromech. Microeng. 32 (4) (2022) 045006, http://dx.doi.org/10.1088/1361-6439/ac56ea, Publisher: IOP Publishing.

[34] L.A. Feldkamp, L.C. Davis, J.W. Kress, Practical cone-beam algorithm, J. Opt. Soc. Amer. A 1 (6) (1984) 612–619, http://dx.doi.org/10.1364/JOSAA.1.000612, Publisher: Optica Publishing Group.

[35] J.Y. Buffiere, E. Maire, J. Adrien, J.P. Masse, E. Boller, In situ experiments with X ray tomography: An attractive tool for experimental mechanics, Exp. Mech. 50 (3) (2010) 289–305, http://dx.doi.org/10.1007/s11340-010-9333-7.

[36] J. Lachambre, pyFEDIC, Zenodo, 2024, http://dx.doi.org/10.5281/ZENODO.8298429, URL https://zenodo.org/doi/10.5281/zenodo.8298429.

[37] J. Réthoré, S. Roux, F. Hild, An extended and integrated digital image correlation technique applied to the analysis of fractured samples: The equilibrium gap method as a mechanical filter, Eur. J. Comput. Mech. 18 (3–4) (2009) 285–306, http://dx.doi.org/10.3166/ejcm.18.285-306, Publisher: Taylor & Francis _eprint: https://doi.org/10.3166/ejcm.18.285-306.

[38] A. Mendoza, J. Neggers, F. Hild, S. Roux, Complete mechanical regularization applied to digital image and volume correlation, Comput. Methods Appl. Mech. Engrg. 355 (2019) 27–43, http://dx.doi.org/10.1016/j.cma.2019.06.005.

[39] M.C. Boyce, E.M. Arruda, Constitutive models of rubber elasticity: A review, Rubber Chem. Technol. 73 (3) (2000) 504–523, http://dx.doi.org/10.5254/1.3547602.

[40] S. Dancette, pymilton - Numpy implementation of Hamilton's "explicit equations for the stresses beneath a sliding spherical contact", 1983, 2025, original-date: 2025-10-08T20:00:40Z, URL https://github.com/sdancette/pymilton.

[41] D.T. Nguyen, P. Paolino, M.C. Audry, A. Chateauminois, C. Fretigny, Y. Le Chenadec, M. Portigliatti, E. Barthel, Surface pressure and shear stress fields within a frictional contact on rubber, J. Adhes. 87 (3) (2011) 235–250, http://dx.doi.org/10.1080/00218464.2011.557340, Publisher: Taylor & Francis _eprint: https://doi.org/10.1080/00218464.2011.557340.

[42] E. Maire, V. Carmona, J. Courbon, W. Ludwig, Fast X-ray tomography and acoustic emission study of damage in metals during continuous tensile tests, Acta Mater. 55 (20) (2007) 6806–6815, http://dx.doi.org/10.1016/j.actamat.2007.08.043.